PHYSICAL REVIEW APPLIED **1,** 034002 (2014)

Mass Transport through the Carrier Gas Boundary Layer in Organic Vapor Phase Deposition

Cedric Rolin,[1,2] Byeongseop Song,[1] and Stephen R. Forrest[1*]
[1] *Departments of Electrical Engineering and Computer Science, Physics, and Materials Science and Engineering, University of Michigan, Ann Arbor, Michigan 48109, USA*
[2] *Large Area Electronics Group, IMEC, Kapeldreef, 75, B-3001 Leuven, Belgium*

(Received 4 February 2014; published 15 April 2014)

We investigate the dynamics of molecular transport across the gas boundary layer formed above a cold substrate used in the organic vapor phase deposition of small organic molecules. The boundary layer properties ultimately determine film thickness uniformity and morphology, and material utilization efficiency. We use laser-induced fluorescence to spatially resolve the temperature and the concentration of organic molecules within the boundary layer. Under conditions typically used in organic vapor phase deposition of chamber pressures less than 5 torr, we find that the boundary layer extends to a remarkable distance of over 10 cm from the cooled substrate surface. Analytical and numerical models of molecular transport processes are developed to understand the transport of organic molecules to the substrate. Our models provide insights into conditions required to optimize film uniformity and material utilization efficiency in the growth of organic electronic devices.

DOI: 10.1103/PhysRevApplied.1.034002

I. INTRODUCTION

Organic vapor phase deposition (OVPD), used for the growth of thin films for organic electronic applications [1], employs a hot inert carrier gas to transport molecules from the evaporation source to a cold substrate where they condense into a thin film [2]. Growth by OVPD can be divided into three steps: evaporation from the source cell, transport through the chamber, and physisorption onto the substrate [3]. After exiting the source cell, the mixture is diluted in a stream of supplementary carrier gas and flows towards the substrate in a well-mixed homogeneous plug flow [4,5]. Upon encountering the cold substrate, the carrier gas forms a boundary layer [3]. This stagnant region consists of a concentration gradient of organic species that forces relatively slow molecular diffusion toward the substrate [3,4], making this the growth limiting step. It also determines the molar flow rate $\dot{n}_s$ of organic species reaching the substrate, thereby influencing film morphology. Since organic molecules are convectively lost to the exhaust, diffusion influences the material utilization efficiency (η). Finally, local variations in the diffusive flux at the substrate results in thickness nonuniformities. Consequently, controlling diffusion is essential to achieving the desired layer morphology with both high efficiency and uniformity.

Boundary layer diffusion has previously been analyzed using the one-dimensional Fick equation [3,4] or, alternatively, by numerical simulations solving the momentum, heat, and mass transport dynamics for a particular system geometry [4,6–10]. Experimental measurements of η and the thickness uniformity over the substrate surface demonstrate that numerical modeling provides a qualitative picture of boundary layer diffusion [9]. Considering the complexity of transport phenomena and the numerous assumptions made in the models, a more direct experimental verification is, therefore, desirable. Here, we use laser-induced fluorescence (LIF) to study transport in the boundary layer near the substrate in a pilot production OVPD system [9]. In LIF, a laser beam locally excites organic species dissolved in the carrier gas, resulting in fluorescence emission [5] whose intensity and spectrum allow for real time measurements of the organic concentration c and local gas temperature T. Under conditions typically used in OVPD of chamber pressures less than 1 torr, we find the boundary layer extends to a remarkable distance of over 10 cm from the cooled substrate surface. Our measurements within and above the boundary layer are compared to a numerical model that provides information about diffusion within the boundary layer that leads to optimizing conditions to achieve the highest film uniformity and material utilization. The model is also useful for making quantitative predictions of OVPD dynamics that can be used in the design of high performance growth systems.

This paper is organized as follows. In Sec. II we derive theoretical models used to describe mass transport across the gas boundary layer in OVPD, and to interpret the temperature dependence of gas phase photoluminescence (PL) measurements. In Sec. III, we describe the experimental procedures used to acquire data. Results are then provided in Sec. IV, and discussed in Sec. V. Section VI presents conclusions.

---

[*] stevefor@umich.edu

II. THEORY

A. Gas flow dynamics in the boundary layer

In the source cell, the solid or liquid organic material evaporates at temperature T_e into the carrier gas with volume flow Q_e. The molar flow rate of organic material at the source $\dot{n}_e$ can be controlled as follows [3,4,6,11]. In equilibrium (i.e., at low Q_e), the source flow rate is set by T_e, and is independent of the amount of organic material contained in the source [12]. In the kinetic regime (i.e., at high Q_e), the carrier gas sweeps all evaporated molecules from the source. The pressure range typical for OVPD is from $P_t = 0.5$ to 10 torr, with gas temperatures of $T_t = 350\,°\mathrm{C}$. These conditions correspond to a mean free path $\lambda < 0.5$ mm. This regime is described by a low Knudsen number, $\mathrm{Kn} = \lambda/R_t \ll 1$, where R_t is the OVPD tube radius [4,6]. The conditions in OVPD can, therefore, be treated as a continuum flow. As the average gas velocity in the tube is low ($v_t < 1$ m/s), the flow is laminar with a low Reynolds number Re, and Mach number, yielding a negligible density change due to pressure variations [6], in contrast to significant density changes with temperature. With molar fractions typically $x < 0.001$, the organic solute is highly diluted, and the mass transfer of organic species does not significantly affect fluid flow.

The carrier gas flow is described by the steady-state equations for a compressible Newtonian fluid, viz. [13–16]

$$\vec{\nabla} \cdot (\rho \vec{v}) = 0, \tag{1}$$

$$\rho(\vec{v} \cdot \vec{\nabla})\vec{v} = -\vec{\nabla} p + \vec{\nabla} \cdot [\mu(\vec{\nabla}\,\vec{v} + (\vec{\nabla}\,\vec{v})') - \tfrac{2}{3}\mu(\vec{\nabla} \cdot \vec{v})I] + \rho\vec{g}, \tag{2}$$

$$\rho C_p \vec{v} \cdot \vec{\nabla} T = \vec{\nabla} \cdot (k\vec{\nabla} T), \tag{3}$$

where ρ, $\vec{v}$, p, and T are the carrier gas density, velocity, pressure, and temperature, respectively. Also, μ, C_p, and k are the carrier gas dynamic viscosity, isobaric specific heat, and thermal conductivity, respectively. Finally, $\vec{g}$ is the acceleration of gravity and I is the identity matrix.

In the dilute binary gas flow considered, mass transfer of the organic species is calculated in steady-state assuming mass balance [13,17]:

$$\vec{\nabla} \cdot (\vec{v} c) = \vec{\nabla} \cdot [D\vec{\nabla} c + \alpha c D \vec{\nabla} \ln(T)], \tag{4}$$

where D is the diffusion coefficient of the organic in the carrier gas which varies as $D = D_0 T^n / p$ $(1.5 \le n \le 2)$. Experimental values are available for D_0 and n, or they can be calculated from Chapman-Enskog theory with reasonable accuracy [18]. Also, α is a unitless thermal diffusion factor that can be determined from Chapman-Enskog theory (see the Appendix). It is apparent in Eq. (4) that both concentration and thermal gradients drive organic molecular diffusion.

The carrier gas flow and the transport of the organic species are determined by numerically solving Eqs. (1)–(4) using the COMSOL Multiphysics® (Chemical Engineering module) finite element analysis software. Figure 1(a) shows an axially symmetric view of the OVPD chamber along with the boundary conditions used. The gas enters the growth chamber characterized by a laminar Poiseuille flow with average velocity v_t, carrying a uniform concentration c_t of organic molecules. The tube pressure at the outlet is P_t. The velocity at the chamber walls is $v = 0$. The organic species do not condense on the hot chamber walls, at temperature T_t. On the cold walls (temperature T_s), condensation is simulated by setting a fixed concentration $c_s < c_t$.

To generalize the results, we introduce the following dimensionless parameters [16,19]: $z^* = z/R_t$, $r^* = r/R_t$, $\vec{v}^* = \vec{v}/v_t$, $\rho^* = \rho/\rho_t$, $\theta^* = (T - T_s)/(T_t - T_s)$, $c^* = c/c_t$, $D^* = D/D_t$, and $\mu^* = \mu/\mu_t$. The subscript t defines the value of a parameter measured in the OVPD tube at temperature T_t and pressure P_t, well outside of the boundary layer. The carrier gas flow is also characterized by $\mathrm{Re} = \rho_t V_t R_t / \mu_t = \dot{m}_{\mathrm{cg}} / \pi R_t \mu_t$, the Prandtl number

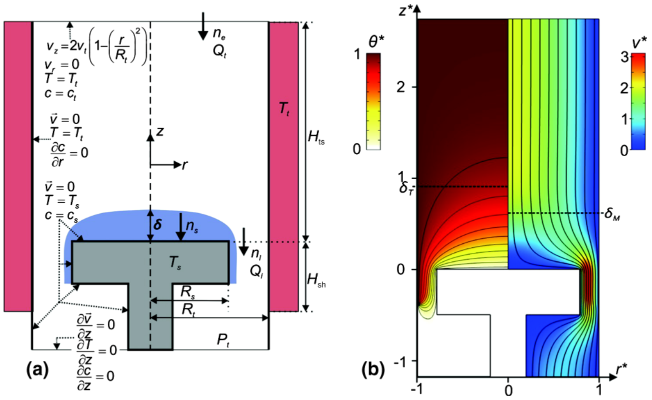

FIG. 1. (a) Schematic of the axial symmetric OVPD tube of radius R_t and height H_t. Dashed arrows give boundary conditions, with the carrier gas velocity and temperature, $\vec{v}$ and T, respectively, and c, the molar concentration of diluted organic species. The molar flow rates of organic materials are $\dot{n}_e$ at the inlet, $\dot{n}_s$ on the substrate, and $\dot{n}_l$ at the exhaust. Q_t and Q_l are the carrier gas volume flows at the inlet and exhaust, respectively, δ is the boundary layer thickness, H_{ts} is the vertical distance between substrate holder (of radius R_s) and the tube inlet, and H_{sh} is the distance between substrate holder and the lower edge of tube heater. (b) Numerical simulation of N_2 flow in the OVPD chamber. Conditions are the following: substrate radius $R_s{}^* = 0.8$, Reynolds number $\mathrm{Re} = 0.35$, Prandtl number $\mathrm{Pr} = 0.73$, and Grashof number $\mathrm{Gr} = 17.5$, corresponding to total mass flow rate $q_{\mathrm{tot}} = 200$ sccm, tube pressure $P_t = 1.5$ torr, tube temperature $T_t = 340\,°\mathrm{C}$, and substrate temperature $T_s = 40\,°\mathrm{C}$ in our experimental OVPD system ($R_t = 125$ mm, $R_s = 100$ mm, $H_{\mathrm{sh}} = 50$ mm). Left: Dimensionless temperature θ^*. Right: Norm of dimensionless velocity v^* along with flow lines.

$\mathrm{Pr} = \mu_t C_{\mathrm{pt}}/k_t$, the Schmidt number $\mathrm{Sc} = \mu_t/D_t\rho_t$, and the Grashof number $\mathrm{Gr} = g\beta\Delta T R_t^3\rho_t^2/\mu_t^2$ [19]. Here, $\dot{m}_{\mathrm{cg}}$ is the carrier gas mass flow rate, β is the carrier gas thermal expansion coefficient, and $\Delta T = T_t - T_s$ is the temperature variation in the growth chamber. A typical carrier gas flow with $\mathrm{Re} = 0.35$, $\mathrm{Pr} = 0.73$, and $\mathrm{Gr} = 17.5$ is shown in Fig. 1(b). The pressure drop is negligible, such that the system is isobaric at pressure P_t. Far above the substrate at $z* > 2$, the flow is an isothermal laminar Poiseuille flow. As it approaches the substrate, the carrier gas forms a stagnation region, or boundary layer, characterized by low velocities and a significant temperature gradient [15,20]. The thickness of the boundary layer is estimated along the chamber axis using [14]

$$\delta_M = aR_s\sqrt{\frac{\mu_i R_s}{\dot{m}_{\mathrm{cg}}}}, \tag{5}$$

where $a \approx 1$ is a geometric constant, R_s is the substrate holder radius, and μ_i is the dynamic viscosity at an intermediate temperature, $T_i = (T_t + T_s)/2$. In Fig. 1(b), ${\delta_M}^* = \delta_M/R_t = 0.62$ with $a = 1$. The thickness of the thermal boundary layer is given by $\delta_T = \delta_M/\,\mathrm{Pr}$. Under most OVPD conditions, $\mathrm{Pr} = 0.6$ to 0.8, implying that $\delta_T > \delta_M$ [16] [see Fig. 1(b) where ${\delta_T}^* = 0.91$]. Because of the low diffusivity of large organic molecules in the carrier gas [18], $\mathrm{Sc} \gg \mathrm{Pr}$. In this case, the boundary layer thickness is $\delta_m = \pi\delta_M/\mathrm{Sc}$ [13].

Now, the macroscopic balance of molar flow rates of organic species is given by

$$\dot{n}_e = \dot{n}_s + \dot{n}_l, \tag{6}$$

where $\dot{n}_l$ is the molar flow rate of organic species lost to the exhaust. Neglecting thermal diffusion, the molar flow rate condensing on the substrate $\dot{n}_s$ is driven by the concentration gradient above the substrate, viz.

$$\dot{n}_s = \pi R_s^2 D_s \frac{\partial c}{\partial z}, \tag{7}$$

where D_s is the diffusion coefficient at the substrate, and z is the distance normal to its surface. Assuming a constant concentration gradient across the boundary layer, Eq. (7) is now

$$\dot{n}_s = \pi R_s^2 \frac{D_i}{\delta_m}(c_\delta - c_s), \tag{8}$$

where D_i is the diffusivity of organic species, and c_δ is the concentration of organic species above the top of the boundary layer at $z = \delta_m$. Under some circumstances, the organic molecules can accumulate above the boundary layer, resulting in ${c_\delta}^* = c_\delta/c_t \geq 1$. At the chamber inlet and at the exhaust at the edge of the substrate, the transport of organic species is convective, and the molar flow rates are given by

$$\dot{n}_e = c_t Q_t = c_t \frac{\dot{m}_{\mathrm{cg}}}{\rho_t}, \tag{9}$$

$$\dot{n}_l = c_l Q_l = c_l \frac{\dot{m}_{\mathrm{cg}}}{\rho_i} = \frac{c_\delta}{b}\frac{\dot{m}_{\mathrm{cg}}}{\rho_i}, \tag{10}$$

where ρ_i is the carrier gas density, and c_l is the molar concentration of the organic solute at the exhaust. Now, c_l cannot be determined from the boundary conditions alone, and hence we introduce b in Eq. (10). Numerical simulations show that $b \sim \sqrt{T}$ and has a weak linear increase with ${R_s}^*$.

Equations (5)–(10) are combined assuming that the organic concentration on the substrate is $c_s = 0$, corresponding to a unity sticking coefficient that is valid for $T_s \ll T_e$. Thus, we obtain the accumulation ratio ${c_\delta}^* = c_\delta/c_t$ above the boundary layer:

$$c_\delta^* = \left(\frac{1}{b\rho_i^*} + \frac{D_i^*}{a}\sqrt{\frac{R_s^*}{\pi\,\mathrm{Re}\mu_i^*}}\right)^{-1}. \tag{11}$$

The first term accounts for the loss of molecules to the exhaust, whereas the second term is determined by diffusion across the boundary layer. An increase of either term results in a lower accumulation of organic species above the boundary layer. Hence, we derive the material utilization efficiency $\eta = \dot{n}_s/\dot{n}_e$:

$$\eta = \left(\frac{a}{b\rho_i^* D_i^*}\sqrt{\frac{\pi\,\mathrm{Re}\mu_i^*}{R_s^*}} + 1\right)^{-1}. \tag{12}$$

The efficiency is independent of pressure, and decreases with increasing Re. Note that η slowly increases with T and strongly with ${R_s}^*$.

B. Temperature dependence of gas phase photoluminescence intensity

We now consider the temperature dependence of the gas phase molecular photoluminescence (PL) intensity. This allows for the interpretation of the LIF signal in the temperature gradient within the boundary layer. The optical power of the fluorescence signal S_F is [21]

$$S_F = \frac{I(\nu)}{h\nu} AlN\sigma(\nu, T)\Phi(T)\frac{\Omega}{4\pi}\eta_d, \tag{13}$$

where ν is the light frequency, $I(\nu)$ is the incident laser irradiance, A and l are, respectively, the cross-sectional area and the length of the excited region, h is Planck's constant, N is the population of molecules in the ground state, $\sigma(\nu, T)$ is the absorption cross section, $\Phi(T)$ is the fluorescence quantum yield, Ω is the collection solid angle, and η_d is the detection efficiency. Obtaining N from measurements of S_F requires knowledge of the gas temperature $\sigma(\nu, T)$ and $\Phi(T)$. In the gas phase, the absorption of luminescent organic materials is reduced, and the peaks broaden towards the red with temperature [22]. Consequently, $\sigma(\nu, T)$ may either increase or decrease, depending on the laser wavelength relative to the absorption peak. A decrease of $\Phi(T)$ with increasing T has often been observed in polycyclic aromatic hydrocarbons, both in the liquid and vapor phases [23–25]. This decrease has been attributed to a thermally activated nonradiative decay rate k_{nr} of the excited state. Its temperature dependence with activation energy E_a follows

$$\Phi(T) = \frac{k_r}{k_r + k_{\mathrm{nr}}^0 \exp(\frac{-E_a}{kT})}, \tag{14}$$

where k_r is the radiative decay rate and k_{nr}^0 is a constant. In interpreting our intensity data, therefore, we use Eqs. (13) and (14).

III. EXPERIMENT

The boundary layer is studied in the OVPD system [9] of radius $R_t = 0.125$ m, illustrated in Fig. 2. The substrate holder is a black anodized Al disk of radius $R_s = 0.1$ m ($R_s{}^* = 0.8$) mounted on a vertical positioning system. The substrate temperature is actively controlled from $T_s = 40$ to 85 °C using chilled water, as measured by a K-type thermocouple mounted on the upper surface of the disk. The region within and above the boundary layer is probed by varying the substrate height H_{ls} relative to the laser beam, from a fully retracted position at $H_{\mathrm{ls}} = 350$ mm, up to 5 mm.

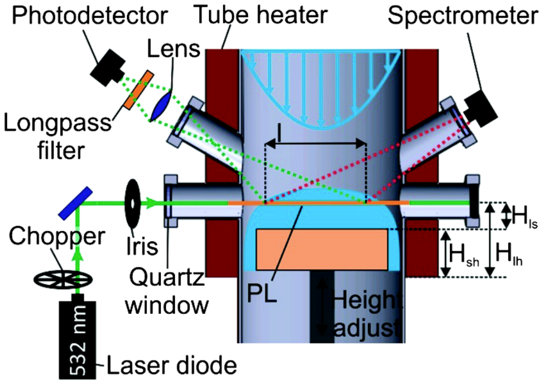

FIG. 2. Schematic of the OVPD tube along with the laser induced fluorescence monitor. Here, PL is the photoluminescence, $l = 150$ mm is the observation distance, H_{ls} is the distance between the laser beam and substrate surface, and H_{lh} is the distance between the laser beam and lower edge of the tube heater. The distance between substrate surface and lower edge of tube heater is $H_{\mathrm{sh}} = H_{\mathrm{lh}} - H_{\mathrm{ls}}$.

The OVPD tube is much longer than R_t, ensuring the full development of Poiseuille flow of the N_2 carrier gas loaded with a homogenized plug flow of the diluted organic material, boron subphthalocyanine chloride (SubPc) [5]. The SubPc (molar density of the solid film, $\rho_M = 3770$ mole/m^3) is evaporated at $T_e = 310$ °C and injected into the OVPD tube with a N_2 mass flow rate of $q_s = 50$ to 100 sccm. The evaporation rate is monitored by a quartz crystal microbalance mounted upstream of the LIF setup. Upon injection into the main tube, SubPc is further diluted in N_2, resulting in a total carrier gas mass flow rate of $100 < q_{\mathrm{tot}} < 800$ sccm. A throttle valve controls the tube pressure in the range $0.5 < P_t < 5$ torr. The tube temperature is maintained at $T_t = 340$ °C, except during spectral broadening and quantum yield calibrations. When the substrate is fully retracted, the gas temperature in the center of the chamber at the height of the laser beam T_l is measured using both a thermocouple and a fluorescence thermometer based on the measurement of emission lifetime from a ruby crystal [26]. Neither technique is, however, able to provide reliable measurements within the boundary layer itself.

For each set of experimental conditions, the molar flow rate of material reaching the substrate $\dot{n}_{s,\mathrm{exp}}$, is measured by placing a Si substrate on the holder and depositing a thin (~30 nm) organic film.

To excite PL in SubPc, the gas mixture is pumped by a Nd:YAG laser at a wavelength of 532 nm with a maximum intensity of 1 W. The PL intensity S_F, from which the organic concentration is inferred, is detected by a photodiode angled towards the center of the substrate to observe a region of length $l \sim 150$ mm centered on the tube axis. A spectrometer (USB4000-FL, Ocean Optics) is mounted on a second angled optical port to measure the emission spectrum. From S_F and the emission spectra, we extract average values of c and T over the optical path length l.

Measurements by LIF are carried out as follows. The SubPc is heated to T_e in the source. The carrier gas flow in the tube is set to desired values of q_{tot}, P_t, and T_t. The substrate temperature is stabilized at T_s. Then, a square pulse of SubPc is injected into the main tube by opening and closing the source plug valve. The pulse duration t_p ranges from 40 to 210 s, such that steady-state conditions are established in the chamber [5]. During the pulse, and for 120 s after, the PL intensity and emission spectrum are continuously recorded. This procedure accurately provides the baseline signal and the steady-state intensity.

IV. RESULTS

To calibrate the temperature dependence of the SubPc PL yield and spectral width, the substrate is retracted to $H_{\mathrm{ls}} = 350$ mm, and the tube temperature in the vicinity of the LIF system is varied from $T_t = 200$ to 450 °C. Then q_{tot} is decreased from 200 to 150 sccm to compensate for the density drop, and to maintain a constant volumetric

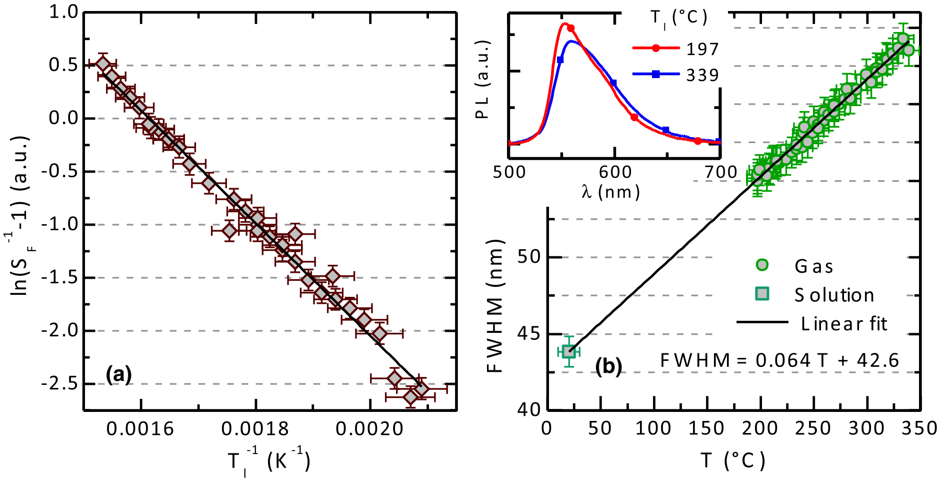

FIG. 3. Evolution of SubPc PL yield and spectral width vs gas temperature T_l, following 60 s long SubPc pulses evaporated at $T_e = 310\,^\circ\mathrm{C}$ and injected into the OVPD tube at pressure $P_t = 1.5$ torr. The tube temperature is increased from $T_t = 200$ to $450\,^\circ\mathrm{C}$ while the total carrier gas mass flow q_{tot} is lowered from 200 to 150 sccm to keep organic concentration constant in the gas. (a) Variation of $\ln(S_F^{-1} - 1)$ with T_l^{-1} where S_F is the measured PL intensity, showing a linear fit to the data (line). (b) Variation of spectrum full width at half maximum (FWHM) as a function of T_l (circles). The square is the FWHM of a SubPc emission spectrum in a benzene solution. The line is a linear fit. Inset: SubPc emission spectra in gas phase at $T_l = 197$ and $339\,^\circ\mathrm{C}$.

flow Q_t. These conditions yield a constant molar concentration $c_t = \dot{n}_e/Q_t$, according to Eq. (9). Then, by injecting pulses of SubPc, the PL intensity and emission spectrum are measured vs gas temperature T_l. We find from Fig. 3(a) that S_F decreases by 50% when T_l increases from 200 to $350\,^\circ\mathrm{C}$, with the linear fit (line) yielding $E_a = 0.46 \pm 0.01$ eV and intercept of 8.6 ± 0.2. As T increases, the PL spectra [inset, Fig. 3(b)] broaden linearly towards the red, as shown in Fig. 3(b).

The gas temperature profile above the substrate, with $q_{\mathrm{tot}} = 200$ sccm, $P_t = 1.5$ torr, $T_s = 40\,^\circ\mathrm{C}$, $T_t = 340\,^\circ\mathrm{C}$, is shown in Fig. 4. When the substrate is fully retracted, T_l reaches a maximum of $290\,^\circ\mathrm{C}$ that is well below tube temperature $T_t = 340\,^\circ\mathrm{C}$. This discrepancy is caused by the cold chamber walls that affect the temperature distribution when the substrate is retracted below the laser probe. This effect is simulated by fixing the heater height relative to the laser H_{lh}, while varying its height relative to the substrate H_{sh} in Figs. 1(a) and 2. The dashed line in Fig. 4 shows the simulated temperature profile with heaters extending below substrate at a fixed $H_{\mathrm{sh}} = 50$ mm (i.e., a variable $H_{\mathrm{lh}} = H_{\mathrm{ls}} + 50$ mm). The solid line shows the profile with $H_{\mathrm{lh}} = 50$ mm (i.e., a variable $H_{\mathrm{sh}} = 50\ \mathrm{mm} - H_{\mathrm{ls}}$). Up to $H_{\mathrm{ls}} = 50$ mm, both lines fit the experimental data. Above that, only a fixed H_{lh} gives a good fit.

Applying Eq. (14) to the measured temperature profiles, and using the results from Fig. 3, the variation of $\Phi(T)$ across the boundary layer is inferred. Then S_F vs H_{ls} in the boundary layer is corrected using Eq. (13), thereby giving the relative concentration of the organic species. To obtain absolute values of the organic concentration c, we use the $\dot{n}_{s,\mathrm{exp}}$ extracted from the thickness measurement of the deposit for each set of experimental conditions. Equation (7) is used to obtain the concentration gradient adjacent to the substrate $(\partial c/\partial z)$ assuming the boundary condition $c_s = 0$ at $H_{\mathrm{ls}} = 0$. The slope is then used to calibrate the concentration profiles measured in the

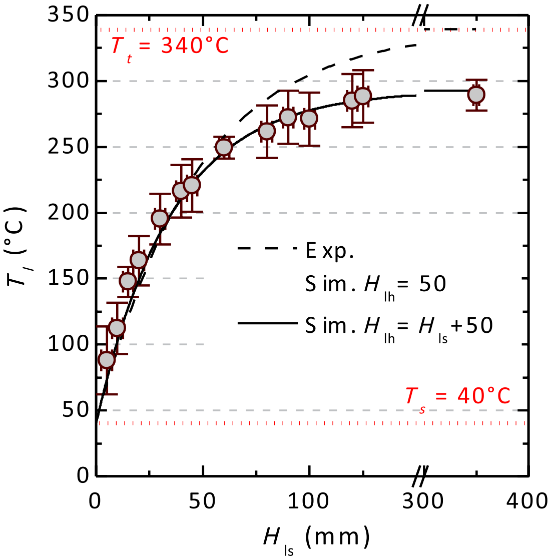

FIG. 4. Gas temperature T_l vs laser beam height relative to substrate H_{ls}. The experimental data are acquired from the SubPc spectral broadening with the following flow conditions: total mass flow rate $q_{\mathrm{tot}} = 200$ sccm, tube pressure $P_t = 1.5$ torr, tube temperature $T_t = 340\,^\circ\mathrm{C}$, substrate temperature $T_s = 40\,^\circ\mathrm{C}$, SubPc evaporation temperature $T_e = 310\,^\circ\mathrm{C}$, mass flow rate of N_2 in the source $q_s = 100$ sccm. The lines are T_l profiles from numerical simulation with $H_{\mathrm{lh}} = 50$ mm (solid) and $H_{\mathrm{lh}} = H_{\mathrm{ls}} + 50$ mm (dashed line). Conditions are similar to that simulated in Fig. 1(b).

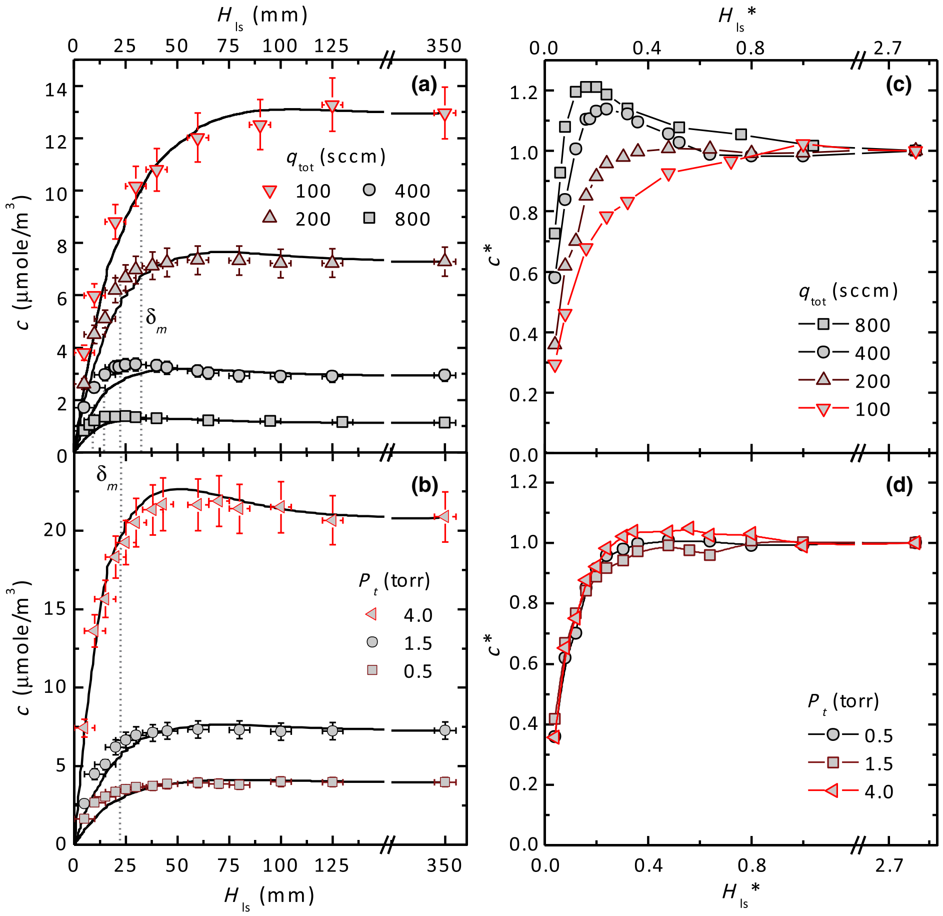

FIG. 5. Concentration of organic material c averaged over the observation distance $l = 150$ mm as a function of laser beam height relative to substrate H_{ls} with (a) a variable total carrier gas mass flow rate q_{tot} and a fixed tube pressure $P_t = 1.5$ torr, and (b) a fixed $q_{tot} = 200$ sccm and a variable P_t. Other conditions are as in Fig. 4. The lines are numerical simulations assuming $H_{lh} = 50$ mm. The diffusivity of SubPc is 18.5 cm^2/s at $T = 340\,°\mathrm{C}$ and $P = 1.5$ torr, and varies as $T^{1.9}/P$. Thermal diffusion is neglected. The inlet organic concentration c_t is set to the concentration $c_{t,\mathrm{exp}}$ measured by experiment at $H_{ls} = 350$ mm. (c) and (d): Same data as in (a) and (b) in dimensionless units. $c^* = c/c_{t,\mathrm{exp}}$, $H_{ls}* = H_{ls}/R_t$, with chamber radius $R_t = 125$ mm.

boundary layer, and to extract the concentration far from the substrate $c_{t,\mathrm{exp}}$. Figures 5(a) and 5(b) show the organic concentration profiles measured for various q_{tot} and P_t, respectively. As previously, $c_{t,\mathrm{exp}}$ is proportional to both $1/q_{tot}$ and P_t [5]. The lines in Figs. 5(a) and 5(b) are the numerically simulated profiles (averaged over the observation length) with $H_{lh} = 50$ mm. The diffusion coefficient is $D_{\mathrm{SubPc,N_2}} = D_0 T^{1.9}/P = 18.5$ cm^2/s, measured at $T = 340\,°\mathrm{C}$ and $P = 1.5$ torr [18]. Thermal diffusion is neglected ($\alpha = 0$). The only fitting parameter used in the simulations is the inlet concentration c_t, adjusted to $c_{t,\mathrm{exp}}$.

The c^* profiles are shown in Figs. 5(c) and 5(d) as functions of q_{tot} and P_t, respectively. Here, the accumulation of organic material near the substrate is apparent. The peak concentration $c_\delta{}^*$, that characterizes the accumulation, increases with q_{tot}, and shows a slight increase with P_t. The phenomenon is also observed in Fig. 6, where c is calculated with the same conditions as in Figs. 1(b) and 4. Figure 6 also maps the diffusive and convective fluxes of the organic species. The convective transport that dominates the flow far above the substrate is replaced by diffusive transport in the boundary layer. Mass transport is characterized by both convection and diffusion as organic material condenses on the cold substrate holder side walls in the region between the substrate holder and chamber wall.

The material utilization efficiency is given by the ratio between $\dot{n}_{s,\mathrm{exp}}$ and $\dot{n}_{s,\mathrm{exp}} = c_{t,\mathrm{exp}} Q_t$ [cf. Eq. (9)]. In Fig. 7 we show η vs q_{tot}, P_t, and T_s. Here, $\eta \sim 40\%$ agrees with previous measurements that compared the mass of the organic species condensed on the substrate to that evaporated from the source [9]. Figure 7 also shows the evolution of $c_\delta{}^*$ with the process parameters q_{tot} q_{tot}, P_t, and T_s. Here, $c_\delta{}^*$ is calculated assuming the substrate is in the hot zone (at $H_{sh} = 50$ mm) using experimental values of $c_{t,\mathrm{exp}}$ for the concentration at the inlet. Equations (11) and (12) used for the fits in Fig. 7(a) yield $a = 1.26 \pm 0.02$ and

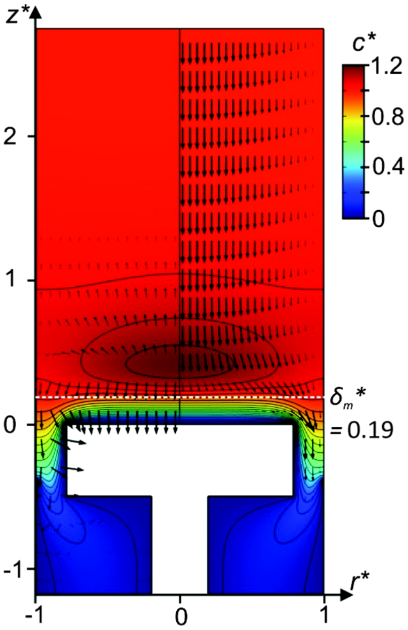

FIG. 6. Organic concentration c^* in the OVPD chamber calculated for $P_t = 1.5$ torr, $q_{\mathrm{tot}} = 200$ sccm, $c_t = 7.5$ μmole/m^3, and $H_{\mathrm{sh}} = 50$ mm. Other conditions are the same as in Figs. 1(b), 4, and 5. The arrows in the left and right panels depict, respectively, the relative diffusive and convective fluxes of the organic species. Also, $\delta_m{}^*$ is the thickness of the dimensionless mass boundary layer.

$b = 1.1 \pm 0.1$. Further, fits in Fig. 7(c) assume $b \sim \sqrt{T}$. Finally, $\delta_m{}^*$ is measured by using $\dot{n}_{s,\mathrm{exp}}$ and c_δ in Eq. (8), assuming a unity sticking coefficient $c_s = 0$. The evolution of $\delta_m *$ with q_{tot}, P_t, and T_s is shown in Fig. 7. Fitting the data in Fig. 7(a) using $\delta_m = \pi\delta_M/\mathrm{Sc}$ with $\mathrm{Sc} = 14.7$, gives $a = 1.26 \pm 0.05$. Values of δ_m are also shown in Figs. 5 and 6.

V. DISCUSSION

When the substrate is lowered below the heaters (i.e., $H_{\mathrm{ls}} > H_{\mathrm{lh}}$), the cold surrounding walls affect both T and c. Consequently, the experimental profiles in Figs. 4 and 5 are not the actual profiles above the substrate during thin film growth when the substrate holder is in the hot zone (i.e., at $H_{\mathrm{ls}} < H_{\mathrm{lh}}$ and $H_{\mathrm{sh}} > 0$). When the actual heater geometry and location are taken into account by fixing H_{lh} and varying H_{sh}, the calculated profiles provide the fits in Fig. 4 without the use of fitting parameters, and in Fig. 5 with only the scaling factor $c_{t,\mathrm{exp}}$ at the inlet used as a parameter. The absence of fitting parameters provides evidence of the accuracy of the numerical model for the determination of mass transport in OVPD. At $H_{\mathrm{sh}} > 0$ (i.e., the substrate holder is in the hot zone), the model can provide quantitative predictions of the transport dynamics, as shown in Figs. 1(b) and 6.

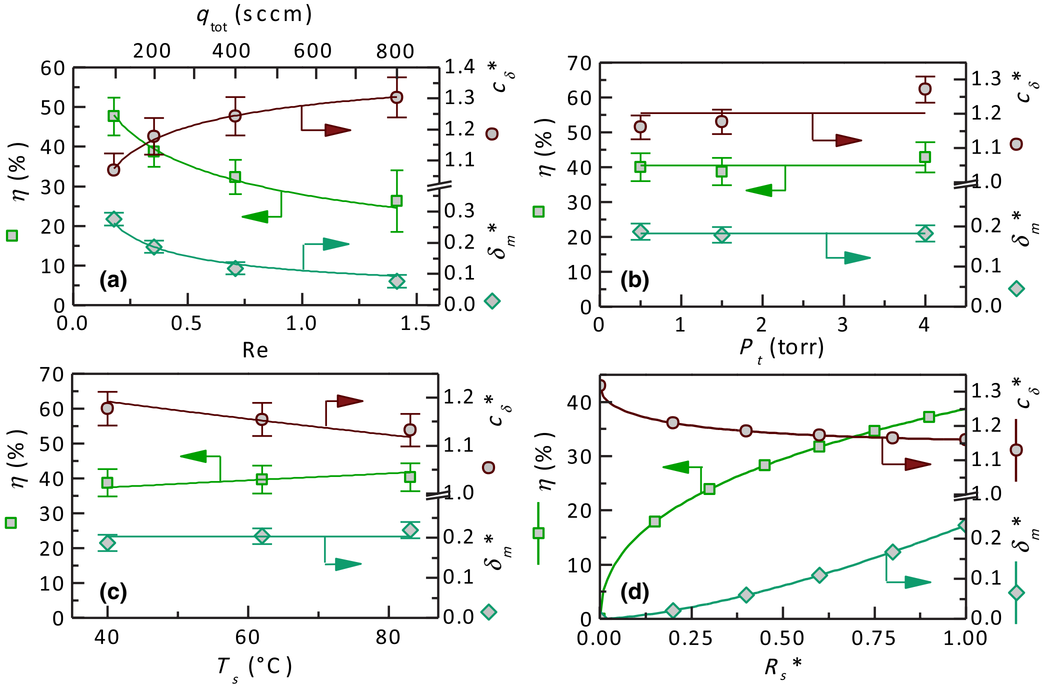

FIG. 7. Material utilization efficiency η, organic molecular concentration $c_\delta{}^*$ accumulated above the boundary layer, and thickness of the mass boundary layer $\delta_m{}^*$ as a function of (a) total carrier gas mass flow rate q_{tot} at pressure $P_t = 1.5$ torr and substrate temperature $T_s = 40\,°\mathrm{C}$, (b) P_t with $q_{\mathrm{tot}} = 200$ sccm and $T_s = 40\,°\mathrm{C}$, (c) T_s with $q_{\mathrm{tot}} = 200$ sccm and $P_t = 1.5$ torr. Other conditions are as in Figs. 4 and 5. The solid lines are fits to the data. (d) Variation of η, $c_\delta{}^*$, and $\delta_m{}^*$ with tube radius $R_s{}^*$, simulated using the same process conditions.

Equation (4) considers diffusion driven by both concentration and thermal gradients. For concentration-driven diffusion, the calculations used [18] of $D_{\mathrm{SubPc,N_2}} \sim T^{1.9}/P$. In the case of thermally driven diffusion, we derive $\alpha_{\mathrm{SubPc,N_2}} = 0.46$ from Chapman-Enskog theory (see the Appendix) [17]. Numerical simulations using $\alpha_{\mathrm{SubPc,N_2}}$, however, show a very limited contribution (<1%) due to thermal processes and hence its effect can be neglected; a conclusion supported by the correspondence between calculated and measured values of c in Fig. 5. This finding also validates the assumption of $c_s = 0$ at the substrate, corresponding to a unity sticking coefficient when $T_s \ll T_e$.

The cooling of the carrier gas near the substrate yields a decrease of $D_{\mathrm{SubPc,N_2}}$ and a loss of volume flow to the exhaust where $Q_l < Q_t$, and hence a lower $\dot{n}_l$ [see Eq. (10)]. Cooling leads to accumulation of organic molecules above the boundary layer, as shown in Figs. 5(c), 5(d), and 6. In turn, accumulation enhances diffusive transport to the substrate and loss to the exhaust, resulting in a reequilibration of the mass balance. In Fig. 7(a), the concentration at the boundary $c_\delta{}^*$ increases with q_{tot} up to 1.3 (i.e., c_δ is 30% higher than inlet concentration c_t), as the organic solute is convectively pushed closer to the substrate holder. Also, $c_\delta{}^*$ increases with P_t due to gravity, and decreases with T_s due to enhanced diffusivity [Figs. 7(b) and 7(c), respectively].

Figure 6 also shows that $c_\delta{}^*$ reaches a maximum in the center of the chamber, whose radial distribution is plotted in Fig. 8. Here, we compare two chamber geometries: one with a short distance between chamber inlet and substrate holder, $H_{\mathrm{ts}}{}^* = 0.6$, and one with $H_{\mathrm{ts}}{}^* = 2.8$, corresponding to situations in Figs. 1(b) and 6. Figure 8(a) shows that a small $H_{\mathrm{ts}}{}^*$ results in a flat concentration profile across the chamber. In both cases, the mass transport boundary layer thickness, corresponding to the position above the substrate where diffusive transport becomes dominant, is decreased by a factor >4 from the center to the edge of the substrate holder. The pinning of the boundary layer to the edge of the substrate results in an enhanced deposition rate near that point, as apparent in Fig. 8(b). The substrate diameter must be smaller than that of the holder to avoid thickness nonuniformities in the deposit from center to edge. In the case of a large $H_{\mathrm{ts}}{}^*$, the radial decrease in concentration compensates the pinning of $\delta_m{}^*(r)$. Hence, accumulation of the organic molecules above the substrate can lead to improved film thickness uniformity.

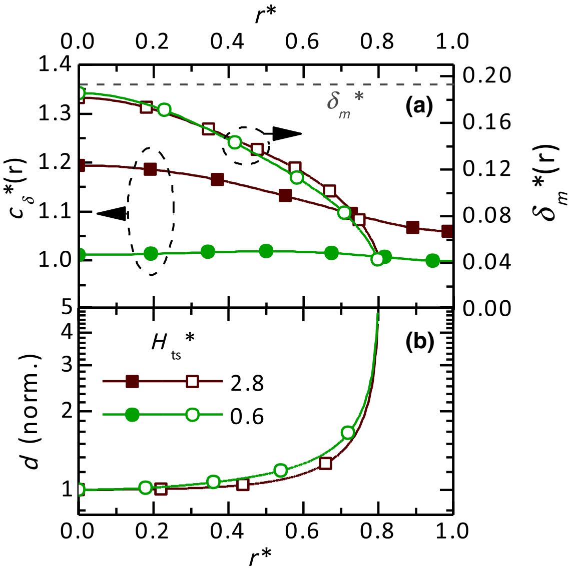

FIG. 8. Radial dependence of organic concentration above the boundary layer $c_\delta{}^*(r)$, mass transfer boundary layer thickness $\delta_m{}^*(r)$, and normalized film thickness profile d for two inlet-substrate heights $H_{\mathrm{ts}}{}^*$. Simulation conditions are as in Figs. 1(b) and 6, with a substrate holder radius $R_s{}^* = 0.8$.

Fitting the experimental variations of η, $c_\delta{}^*$, and $\delta_m{}^*$ in Fig. 7 with the analytical model provides values for geometrical parameters a and b. In Fig. 7(d), the model is then used to predict the influence of substrate radius $R_s{}^*$ on the boundary layer. Maximizing the material use efficiency requires a large substrate, as the ratio between diffusion to the substrate and convective loss increases. Also, $\delta_m{}^*$ increases with $R_s{}^*$ since thicker boundary layers develop on larger substrates.

Our results show that under conventional conditions employed in OVPD, the boundary layer extends to a stagnation point at a remarkably long distance from the substrate. We note that OVPD system designs have been implemented using a shower head placed within the boundary layer to finely control the gas distribution, and to maximize both η and the thickness uniformity [6,8,27]. Figure 9 shows the dependence of η and film thickness uniformity [given by the standard deviation in layer thickness stdev(d)] on the height of the shower head and the substrate radius. At large $H_{\mathrm{ts}}{}^*$, substrates with a diameter close or equal to that of the substrate holder (i.e., $R_w{}^* = R_s{}^* = 0.8$), exhibit a low uniformity that is strongly affected by edge pinning. By reducing the shower-head–substrate gap, however, both η and uniformity improve. For example, stdev(d) <3% for $R_w{}^* = 0.75$ when $H_{\mathrm{ts}}{}^* < \delta_m{}^*$. In consequence, the shower head optimizes film deposition when placed within the mass transport boundary layer.

Finally, we investigated the influence of gravity on gas flow. The occurrence of natural convection in the OVPD chamber is quantified by the ratio of dimensionless numbers $\mathrm{Gr}/\mathrm{Re}^2 = g\beta\Delta T R_t/v_t^2$, that approximates the ratio between buoyancy and inertial driving forces [19]. Natural convection is encouraged by an increased temperature drop ΔT, larger chamber size R_t, and lower gas velocities v_t. For Fig. 1(b) where $\mathrm{Gr}/\mathrm{Re}^2 = 144$, the effect of gravity is limited. Gravity has more impact, however, when pressure is increased to $P_t = 4.0$ torr, where $\mathrm{Gr}/\mathrm{Re}^2 = 1024$. Figure 10 shows the organic concentration c^* and the flow streamlines at 4.0 torr in the presence

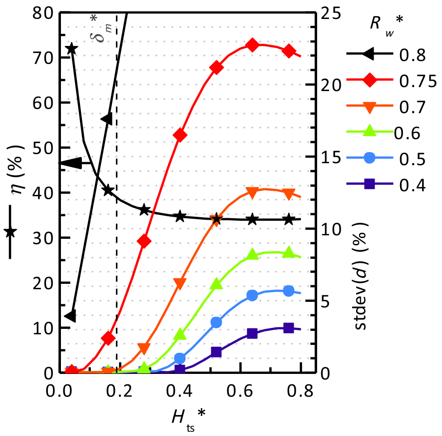

FIG. 9. Influence of the shower-head-to-substrate height $H_{ts}{}^*$, on material utilization efficiency η and standard deviation in film thickness stdev(d). Here, $R_w{}^*$ is the substrate radius. Simulations assume the same conditions as in Figs. 1(b) and 6, with substrate holder radius $R_s{}^* = 0.8$, but using a square velocity profile for the carrier gas at the inlet.

and absence of gravitational effects, for two different substrate orientations (i.e., deposition upwards or downwards). It is apparent from Figs. 10(b) and 10(c) that gravity results in an increased material accumulation in the boundary region. The value of $\mathrm{Gr}/\mathrm{Re}^2$ at which natural convection becomes non-negligible depends on system orientation, as is apparent from Figs. 10(a) and 10(c). In our OVPD configuration where the substrate faces upward [Fig. 10(c)], gravity forces the cooling gas along the direction of flow, thereby slightly reducing the boundary layer thickness. When the substrate faces downwards [Fig. 10(a)], densified gas is pulled back upstream along the tube axis, thereby creating a convective cell that increases the boundary layer thickness and reduces η.

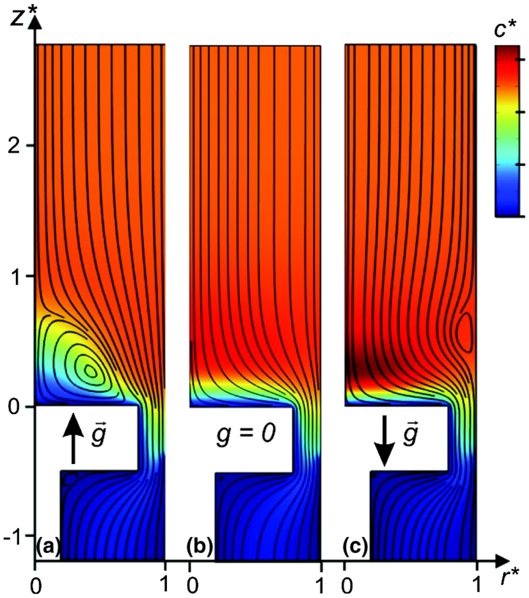

FIG. 10. Effect of gravity on organic concentration c^*. Also shown are streamlines of the gas flow. (a) Acceleration of gravity $\vec{g}$ pointing up and $g = 9.81\ \mathrm{m}^2/\mathrm{s}$, (b) $g = 0\ \mathrm{m}^2/\mathrm{s}$, and (c) $\vec{g}$ pointing down relative to the substrate. Simulation conditions are as in Figs. 1(b) and 6, except $P_t = 4.0$ torr.

VI. CONCLUSIONS

We use a combination of analysis and experiment to study gas dynamics in the boundary layer formed above the substrate in OVPD. We find that the boundary layer is characterized by significant temperature and concentration gradients extending over large distances that drive molecular diffusion to the substrate. This rate-limiting diffusion process determines film morphology, material utilization efficiency, and thickness uniformity. Diffusion is driven by gas concentration gradients generated by the presence of a cold substrate within the heated gas flow stream.

As the gas cools in the vicinity of the substrate, convective losses to the exhaust are reduced. This phenomenon, along with slow diffusion through the boundary layer, form a bottleneck to mass transport that results in the significant accumulation of organic molecules at the entrance to the boundary layer. Surprisingly, this accumulation results in a higher film thickness uniformity. A second approach to achieve thickness uniformity and material utilization efficiency is the use of a shower head that is optimally positioned within the boundary layer itself. Finally, convection and concentration gradients are strongly influenced by gravity at low gas velocities, achieved at high pressure or low flow rates.

ACKNOWLEDGMENTS

We thank Professor Richard Lunt at Michigan State University for useful discussions. We are grateful to the SunShot Program of the U.S. Department of Energy (EERE) under Grant No. DE-EE0005310 (B. S., experiment, C. R., experiment, analysis) and Universal Display Corp. (C. R., LIF) for partial financial support of this work. This work was also supported by the U.S. Department of Energy (DOE), Office of Basic Energy Sciences, as part of the Center for Energy Nanoscience, Energy Frontier Research Center, Grant No. DE-SC0001013 (S. R. F., analysis).

APPENDIX: THERMAL DIFFUSION

In a binary gas with a temperature gradient, thermal diffusion forces heavier molecules towards the cold zone [16]. In the case of a highly diluted mixture, Chapman-Enskog theory gives the thermal diffusion factor as [17]

$$\alpha \simeq \frac{5\sqrt{2}}{8}\left(\frac{\sigma_{12}}{\sigma_2}\right)\left(\frac{6\Omega_{12}^{(1,2)^*} - 5\Omega_{12}^{(1,1)^*}}{\Omega_2^{(2,2)^*}}\right)\left(1 - \frac{3M_2}{2M_1}\right), \qquad \text{(A1)}$$

where σ_{12} is the average molecular diameter, σ_2 is the diameter of the carrier gas molecules, $\Omega^{(l,k)^*}$ are dimensionless collision integrals [28], and $M_1 \gg M_2$ are the molar masses of the organic species and the carrier gas, respectively. The importance of thermal diffusion is estimated from its ratio to that in the absence of thermal diffusion [17]:

$$\frac{J}{J_{\alpha=0}} = \alpha\left(\frac{\ln(T_s/T_\delta)}{(T_s/T_\delta)^\alpha - 1}\right), \tag{A2}$$

where T_s is the substrate temperature and T_δ is the temperature at the entrance to the momentum boundary layer. In the case of SubPc in N_2, we find $\alpha_{\mathrm{SubPc,N_2}} = 0.46$ at $T_i = 157\,°\mathrm{C}$, and $J/J_{\alpha=0} = 1.08$ with $T_s = 40\,°\mathrm{C}$. Therefore, we infer that diffusive transport is enhanced by 8%, whereas numerical simulations show that the enhancement is <1%.

[1] S. R. Forrest, The path to ubiquitous and low-cost organic electronic appliances on plastic, Nature (London) **428**, 911 (2004).

[2] M. A. Baldo, M. Deutsch, P. Burrows, H. Gossenberger, M. Gerstenberg, V. Ban, and S. R. Forrest, Organic vapor phase deposition, Adv. Mater. **10**, 1505 (1998).

[3] M. Shtein, H. F. Gossenberger, J. B. Benziger, and S. R. Forrest, Material transport regimes and mechanisms for growth of molecular organic thin films using low-pressure organic vapor phase deposition, J. Appl. Phys. **89**, 1470 (2001).

[4] M. Shtein, in *Organic Electronic Materials and Processes. Devices and Applications*, edited by F. So (CRC Press, Boca Raton, FL, 2009), pp. 27–57.

[5] C. Rolin, G. Vartanian, and S. R. Forrest, Laser induced fluorescence monitoring of the transport of small organic molecules in an organic vapor phase deposition system, J. Appl. Phys. **112**, 113502 (2012).

[6] C. Rolin, *Vapor Phase Deposition of Organic Semiconductors: Application to Field Effect Transistors* (LAP Lambert Academic Publishing, Saarbrücken, Germany, 2010).

[7] M. Shtein, P. Peumans, J. B. Benziger, and S. R. Forrest, Micropatterning of small molecular weight organic semiconductor thin films using organic vapor phase deposition, J. Appl. Phys. **93**, 4005 (2003).

[8] M. Schwambera, N. Meyer, S. Leder, M. Reinhold, M. Dauelsberg, G. Strauch, M. Heuken, H. Juergensen, T. Zhou, T. Ngo, J. Brown, M. Shtein, and S. R. Forrest, Modeling and fabrication of organic vapor phase deposition (OVPD) equipment for OLED display manufacturing, SID Symp. Dig. Tech. Pap. **33**, 894 (2002).

[9] R. R. Lunt, B. E. Lassiter, J. B. Benziger, and S. R. Forrest, Organic vapor phase deposition for the growth of large area organic electronic devices, Appl. Phys. Lett. **95**, 233305 (2009).

[10] C. Rolin, K. Vasseur, J. Genoe, and P. Heremans, Growth of pentacene thin films by in-line organic vapor phase deposition, Org. Electron. **11**, 100 (2010).

[11] G. J. McGraw and S. R. Forrest, Fluid dynamics and mass transport in organic vapor jet printing, J. Appl. Phys. **111**, 043501 (2012).

[12] C. Rolin, K. Vasseur, B. Niesen, M. Willegems, R. Müller, S. Steudel, J. Genoe, and P. Heremans, Vapor phase growth of functional Pentacene films at atmospheric pressure, Adv. Funct. Mater. **22**, 5050 (2012).

[13] R. B. Bird, W. Stewart, and E. Lightfoot, *Transport Phenomena* (Wiley, New York, 2006).

[14] H. Schlichting and K. Gersten, *Boundary-Layer Theory* (Springer, Berlin, Germany, 2000), 8th ed.

[15] R. Mahajan, Transport phenomena in chemical vapor-deposition systems, Adv. Heat Transf. **28**, 339 (1996).

[16] K. F. Jensen, E. O. Einset, and D. I. Fotiadis, Flow phenomena in chemical vapor deposition of thin films, Annu. Rev. Fluid Mech. **23**, 197 (1991).

[17] W. L. Holstein, Thermal diffusion in metal-organic chemical vapor deposition, J. Electrochem. Soc. **135**, 1788 (1988).

[18] C. Rolin and S. R. Forrest, Diffusion coefficients of fluorescent organic molecules in inert gases, Appl. Phys. Lett. **103**, 041911 (2013).

[19] G. Wahl, Hydrodynamic description of CVD processes, Thin Solid Films **40**, 13 (1977).

[20] C. Houtman, D. B. Graves, and K. F. Jensen, CVD in stagnation point flow an evaluation of the classical 1D treatment, J. Electrochem. Soc. **133**, 961 (1986).

[21] I. S. Burns and C. F. Kaminski, Diode laser induced fluorescence for gas-phase diagnostics, Z. Phys. Chem. **225**, 1343 (2011).

[22] A. Thöny and M. J. Rossi, Gas-phase UV spectroscopy of anthracene, xanthone, pyrene, 1-bromopyrene and 1,2,4-trichlorobenzene at elevated temperatures, J. Photochem. Photobiol. A **104**, 25 (1997).

[23] E. J. Bowen and J. Sahu, The effect of temperature on fluorescence of solutions, J. Phys. Chem. **63**, 4 (1959).

[24] M. Komfort, H.-G. Löhmannsröben, and T. Salthammer, The temperature dependence of photophysical processes in perylene, tetracene and some of their derivatives, J. Photochem. Photobiol. A **51**, 215 (1990).

[25] S. Hirayama, Temperature effect on the vapor phase fluorescence in cyano-substituted anthracenes. Reconsideration of the S1-Tn energy gap, J. Am. Chem. Soc. **103**, 2934 (1981).

[26] J. D. Bauer, L. Bayarjargal, and B. Winkler, Ruby fluorescence lifetime measurements for temperature determinations at high (p, T), High Press. Res. **32**, 155 (2012).

[27] M. Heuken and N. Meyer, in *Organic Electronics: Materials, Manufacturing and Applications*, edited by H. Klauk (Wiley, Weinheim, Germany, 2006), pp. 203–232.

[28] P. D. Neufeld, A. R. Janzen, and R. A. Aziz, Empirical equations to calculate 16 of the transport collision integrals $\Omega(l,s)^*$ for the Lennard-Jones (12–6) potential, J. Chem. Phys. **57**, 1100 (1972).